Korean J. Chem. Eng., 38(7), 1460-1468 (2021)
DOI: 10.1007/s11814-021-0780-x

pISSN: 0256-1115
eISSN: 1975-7220

A thixotropic fluid flow around two sequentially aligned spheres

Jaekwang Kim* and Jun Dong Park,***,†**

*Department of Mechanical Science & Engineering, University of Illinois at Urbana-Champaign, Urbana, Illinois, 61801
**Department of Chemical and Biological Engineering, Sookmyung Women's University,
Cheongpa-ro 47-gil 100, Yongsan-gu, Seoul 04310, Korea
***Institute of Advanced Materials and Systems, Sookmyung Women's University,
Cheongpa-ro 47-gil 100, Yongsan-gu, Seoul 04310, Korea
(*Received 20 December 2020 • Revised 2 March 2021 • Accepted 7 March 2021*)

Abstract−We studied the thixotropic-hydrodynamic interaction of particles resulting from a combination of external flow conditions and intrinsic thixotropy of a fluid. As a model system, a low Reynolds number Moore thixotropic fluid flow around two sequentially aligned sphere was simulated using the standard Galerkin finite element method. The drag coefficients of each sphere were used to quantitively characterize the thixotropic-hydrodynamic interaction between the two spheres. First, hydrodynamic interaction change according to the external flow condition was identified at a fixed distance. Subsequently, the parametric analysis was extended to incorporate the effect of the geometrical condition, the sphere-sphere distance parameter. This yields a conceptual map that distinguishes the thixotropic-hydrodynamic interaction into three different types: the geometric hydrodynamic interaction, combination of geometric and local thixotropic interaction, and global thixotropic-hydrodynamic interaction.

Keywords: Thixotropy, Structure-kinetics Model, Hydrodynamic Interaction, Flow Around a Sphere

INTRODUCTION

A distinct rheological phenomenon of "the continuous decrease of viscosity with time when flow is applied to a material that has been previously at quiescent state, and the subsequent recovery of viscosity when flow ceases" is defined as thixotropy [1]. It is ubiquitous in various applications from industrial materials to personal care products. For example, in raw crude oil, thixotropy occurs naturally from a structured solid precipitate known as wax. The thixotropy of crude oil is an important factor that should be considered during the design of drilling and pipe-line transport processes. Meanwhile, thixotropy is intentionally introduced to material or commercial products for the convenience of process control or end use. Thixotropic properties embedded in materials can facilitate manufacturing processes (e.g., coating and printing) and storage by providing both flowability and stability based on the imposed flow condition. Therefore, it is important to understand and utilize the thixotropic property of materials for successful material processing.

As thixotropy becomes more recognized, considerable achievements in characterizing material thixotropy have been realized in the last decades. Understanding the relationship between microstructural changes in a material and its thixotropic rheology is of particular interest in theoretical studies, which has yielded different classes of models: structure-kinetics, continuum mechanics, and micromechanical models [2-7]. Theoretical modeling is particularly significant from a rheological perspective, because it provides useful insights into the physical origins of thixotropy. Experimental approaches aim to characterize the material rheology in terms of material functions under different flow conditions: step shear, shear hysteresis, and shear startup [8]. Most of these typical flow conditions retain the simplest flow scenarios (called rheometric flow), where the shear field is homogeneous.

However, material processes in real applications (in oil/cosmetics/food industries) inevitably involve geometry-induced nonhomogeneous flows, which are not fully benefited from previous studies. This is because fluid elements in a non-homogeneous flow accumulate different shear histories according to path lines. Consequently, the thixotropic material demonstrates not only time-dependence, but also spatial-dependence in actual processes. In this regard, simulation studies aim to extend theoretical studies toward more complicated flow scenarios [9,10]. For example, our previous numerical study, in which we investigated the thixotropic flow around a settling sphere [11], demonstrated that a concept of net viscosity (averaged over the sphere surface) acting on a sphere arises from the balance of three competing factors: Brownian structure recovery, shear-induced structure breakdown, and convection. In general, the balance between the last two factors is significantly influenced by the geometrical factors of the flow.

The combination of intrinsic material thixotropy and flow geometry may lead to a more complicated nonhomogeneous flow that plays a critical role in determining product maturity in various processes, including printing, coating, and mixing. Nevertheless, there is only a handful of studies on nonhomogeneous thixotropic flow in non-trivial geometry, other than rheometric flows [9-12]. This is partly because it is quite tricky to model a thixotropic fluid in a complicated geometry and find a trustworthy numerical solution.

In this work, as a first step to challenging nonhomogeneous thixotropic flow problems in actual processes, we begin with a simple,

†To whom correspondence should be addressed.
E-mail: jk12@illinois.edu, jdpark@sookmyung.ac.kr

conventional example. We will numerically investigate a range of flow and geometric conditions on a purely viscous thixotropic flow around two sequentially aligned spheres. This is in line with a single sphere case in our earlier study [11]. The two-sphere problem involves an additional geometric factor (the distance between the two spheres), that potentially influences the fluid thixotropy. In particular, it is of interest how the hydrodynamic interaction between the two spheres appears in the presence of fluid thixotropy. Hence, we conduct a series of numerical simulations to set a relevant dimensionless parametric space that accounts for the geometrical factor and intrinsic material thixotropy. Aside from theoretical interest, the thixotropic flow around sequentially-aligned spheres is also closely linked with various industrial applications as well. Modeling the rheology of particulate suspensions comprising particles immersed in thixotropic media, such as battery slurry [13,14] is expected to be directly benefited from this study. Additionally, this study will be useful for understanding flow in a packed bed reactor, which contains particulate catalyst and thixotropic reactant fluid as a result of chemical reaction [15-17]. Other applications are channel flows including oil pipeline-transport, printing, coating, and blood flow, where fluid with thixotropy flows around sequentially located obstacles [18-22].

The remainder of this paper is organized as follows. In the background section, a rheological model of generic purely viscous thixotropy fluids, known as structure-kinetics is introduced. Subsequently, the two-sphere model problem is formulated, and the relevant dimensionless numbers are identified. In the following sections, details of the numerical method are provided. The main findings of the present study are discussed in the Results & Discussion. We conclude by summarizing our findings in the Conclusion.

BACKGROUND

1. Thixotropy Description Based on the Structure-kinetics Model

We first introduce the structure-kinetics model [2,3] to describe a generic thixotropic fluid. In the structure-kinetics approach, a dimensionless scalar λ is used to represent the instantaneous state of the material structure. Rheological properties, such as steady-state viscosity, are expressed as a function of λ. The structure parameter λ can evolve depending on the shear history that a material has gone through, and the material exhibits thixotropic behavior (changes in viscosity) based on the evolution of λ. Although the structure-kinetics is limited in yielding a clear connection between the structure parameter λ and the real microstructure of the material, this empirical model has been widely employed to characterize thixotropy originating from different molecular mechanisms.

The structure-kinetics model involves two equations: the kinetic evolution equation for λ, and the correlation equation between λ and the viscosity of a material. We selected a simple linear model-form comprising the following equations. First, the kinetic evolution equation in a flow of velocity **u** is expressed as

$$\frac{d\lambda}{dt}=\frac{\partial\lambda}{\partial t}+(\mathbf{u}\cdot\nabla\lambda)=-k_s\dot{\gamma}_s\lambda+k_a(1-\lambda) \tag{1}$$

where $\dot{\gamma}_s$ is the second-invariant of the strain-rate tensor ($\dot{\boldsymbol{\gamma}}=\nabla\mathbf{u}+(\nabla\mathbf{u})^T$),

$$\dot{\gamma}_s=\sqrt{\frac{\dot{\boldsymbol{\gamma}}:\dot{\boldsymbol{\gamma}}}{2}} \tag{2}$$

In this form, the structure parameter λ is assumed to change between 0 and 1 ($\lambda\in[0, 1]$). λ=0 and λ=1 denote the completely broken structure and full-structured states, respectively. The kinetic evolution equation considers three basic mechanisms for the structure parameter λ change. First, the convection of more or less structured fluid element is denoted by $\mathbf{u}\cdot\nabla\lambda$ in Eq.(1). The remaining terms on the right-hand side ($-k_d\dot{\gamma}_s$ and $k_a(1-\lambda)$) represent shear-induced breakdown and structure rebuilding by thermal motion, respectively. Herein, k_d [-] and k_a [s] are the destruction parameter and Brownian recovery timescale, which indicate the structural sensitivity to the applied shear rate and the rate of Brownian build-up. These two parameters define the characteristic time of the structure formation t_c ($=k_d/k_a$).

Assuming a purely viscous (i.e., non-elastic) thixotropy fluid, the structure parameter λ is correlated to viscosity according to the following equation:

$$\eta(\lambda)=\eta_\infty+\eta_{str}\lambda \tag{3}$$

In Eq. (3), the two parameters η_{str} and η_∞ express the structural contribution to viscosity and the residual viscosity that is observed when the microstructure is completely broken, respectively. The combination of Eqs. (1) and (3) is referred onward as the Moore thixotropy model [3]. The Moore thixotropy model has been widely adopted for theoretical studies of thixotropic fluids as it reveals many important features of thixotropic fluid flow in different flow scenarios, despite its simplicity. The four parameters {k_d, k_a, η_∞, η_{str}} in the Moore thixotropy model are typically determined via rheological measurements obtained using a rheometer. In this study, these parameters were set as shown in Table 1.

In a homogeneous steady shear flow condition, there exists no gradient of λ in **u** direction. Therefore, the homogeneous solution of the structure parameter λ_{ss} can be written as a simple function of t_c as $\lambda_{ss}=1/(t_c\dot{\gamma}+1)$. Subsequently, the steady-state viscosity of the Moore thixotropy model can be obtained by substituting λ_{ss} to Eq. (3), yielding

$$\eta_{ss}(\dot{\gamma})=\eta_\infty+\frac{\eta_{str}}{1+t_c\dot{\gamma}} \tag{4}$$

Fig. 1 shows the steady state viscosity η_{ss}, which is the normalized by viscosity of the full-structured material ($\eta_\infty+\eta_{str}$) as a function of the dimensionless shear rate $t_c\dot{\gamma}$.

2. Formulation

In this part, we formulate the purely viscous thixotropic fluid flow around two sequentially aligned spheres using the structure-kinetics

Table 1. Moore thixotropic model parameters used in this study

η_{str}	49.0 Pa·s
η_∞	1.0 Pa·s
k_a	0.1 s^{-1}
k_d	2.0
t_c ($=k_d/k_a$)	20 s

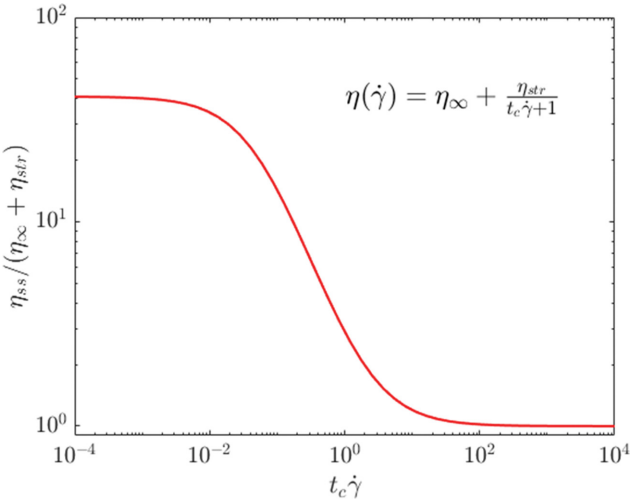

Fig. 1. Steady-state viscosity η_{ss} of the model fluid in simple shear with the model parameters summarized in Table 1. Vertical axis is normalized by viscosity at full-structured state $\eta_{ss}+\eta_{str}$. Abscissa is normalized by the characteristic time of the structure formation t_c ($=k_d/k_a$).

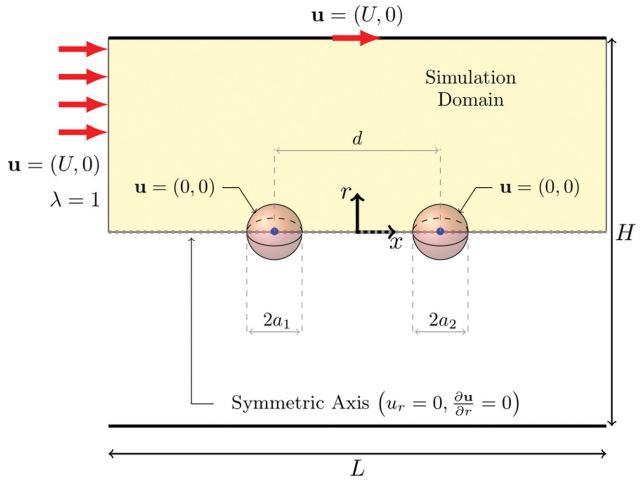

Fig. 2. Schematic representation of two sequentially aligned spheres. Boundary condition for velocity field $\mathbf{u}=(u_x, u_r)$ and the structure parameter λ are notated. The simulation domain Ω for the axisymmetric constraints is colored in yellow.

model. We consider a cylindrical domain Ω' with a sufficiently large size, with dimensions length L and height H, as shown in Fig. 2. The domain Ω' is initially filled with a fully structured fluid ($\lambda(\mathbf{x})=1$), and two spheres (with radius a) are moving with a constant velocity, maintaining a distance of d. Because we are interested in a system where inertia effects are not a practical concern, we assume that viscous force dominates the advective inertia forces, resulting in a Stokes flow ($Re \ll 1$) [23]. The incompressible Stokes flow around two spheres is governed by the momentum and mass conservation equations,

$$\nabla\cdot([\eta_\infty+\eta_{str}\lambda]\dot{\gamma}) - \nabla p = 0, \tag{5}$$

$$\nabla\cdot\mathbf{u} = 0, \tag{6}$$

which are coupled with the steady-state kinetic evolution equation for structure parameter λ,

$$(\mathbf{u}\cdot\Delta\lambda) + k_d\dot{\gamma}_s - k_a(1-\lambda) = 0 \tag{7}$$

and the correlation equation between λ and η (Eq. 3). We assume that the flow is axisymmetric about the x-axis. This enables us to consider the one-half of the domain $r\in[0, H/2]$ as the simulation domain Ω (shown in the yellow shaded region in Fig. 2) with axisymmetric constraints:

$$u_r = 0, \frac{\partial u_r}{\partial r} = 0 \text{ at } r = 0. \tag{8}$$

It is noteworthy that the axisymmetric condition reduces the flow around two spheres to a two-dimensional flow in cylindrical coordinates. The remaining velocity boundary conditions are described in a fixed frame, the origin of which is located at the midpoint of the two spheres.

$$\begin{aligned}&\mathbf{u}=(U, 0) \text{ at } x=\pm L/2\\ &\mathbf{u}=(U, 0) \text{ at } r=H/2\\ &\mathbf{u}=0 \text{ at } (x-d/2)^2+r^2=a^2\\ &\mathbf{u}=0 \text{ at } (x+d/2)^2+r^2=a^2\end{aligned} \tag{9}$$

The first two velocity boundary conditions (with sufficiently large values of H and L) indicate uniform flow at far field. The inlet boundary condition for the advection Eq. (7) is given as

$$\lambda = 1 \text{ at } x = -L/2. \tag{10}$$

3. Dimensionless Numbers for the Model Thixotropic Fluid Flow

For a quantitative characterization of the model thixotropic fluid flow problem, we analyzed the drag coefficient of each sphere. For a sphere in a fluid, the hydrodynamic resistance D is calculated as

$$D = \int_{\partial S} \mathbf{e}_x\cdot(-p\mathbf{I} + [\eta_\infty+\eta_{str}\lambda]\dot{\gamma})\cdot\mathbf{n}\,dA \tag{11}$$

Here, ∂S, $\mathbf{e}_x$, $\mathbf{n}$, and $\mathbf{I}$ indicate the surface element, unit vector in the x-direction, normal vector, and identity tensor, respectively. Subsequently, we define the drag coefficient C_s as

$$C_s = \frac{D}{K\times 6\pi(\eta_\infty+\eta_{str})aU} \tag{12}$$

where the denominator

$$D_{Newtonian} = K\times 6\pi(\eta_\infty+\eta_{str})aU \tag{13}$$

is the Stokesian drag for a single sphere with radius a moving with a small velocity U in a Newtonian fluid of viscosity ($\eta_\infty+\eta_{str}$). Here, K(2a/H) is the side-wall correction factor appearing as a Faxen series for the ratio of the sphere radius to the distance between the wall and sphere [23].

Although a field solution of either the velocity $\mathbf{u}=(u_x, u_r)$, or structure $\lambda(\mathbf{x})$ may contain more detailed information regarding the thixotropic fluid flow, C_s contains implicit information regarding the viscosity distribution around each sphere. When the thixotropy affects to the spheres' motion, the value of C_s will begin to deviate from the Newtonian values and decrease. We used the single metric C_s because it can both intuitively and quantitatively character-

ize the flow at different flow conditions [11]. However, for the two-sphere problem, C_s must be analyzed meticulously because it may also indicate purely geometric interactions (i.e., the presence of other particles) as well as the effect of thixotropy. To isolate the two different factors, we first reviewed the earlier studies regarding each of them.

An important early work on the geometric effect of drag coefficient was first performed by Stimson and Jeffery, who investigated the settling motion of two vertically aligned spheres (also with the same radius a) in a Newtonian fluid [24]. They used a Stokes stream function represented by the curvilinear coordinate in the meridian plane and calculated the analytical solutions for the flow and drag coefficient C_s. The primary conclusion was that the two spheres exhibited the same drag coefficient C_s, which was attributed to the symmetric and reversible nature of Newtonian Stokes flow. The analytical expression for C_s was written in a series form of the inverse hyperbolic cosine of α=arcosh(d/2a) [24], as follows:

$$C_s(\alpha)=\frac{4}{3}\sinh\alpha\sum_{n=1}^{\infty}\frac{n(n+1)}{(2n-1)}\left(1-\frac{4\sinh^2\left(n+\frac{1}{2}\right)\alpha-(2n+1)^2\sinh^2\alpha}{\sinh(2n+1)\alpha+(2n+1)\sinh 2\alpha}\right) \quad (14)$$

In Fig. 3 C_s is plotted as a function of the distance parameter d/2a, which denotes the normalized distance (by their diameter) between the two spheres. In general, the values of C_s are smaller than 1, suggesting that the existence of another particle aids the motion of the others. As d/2a→∞, C_s slowly recovers to one, corresponding to the single sphere case.

On the other hand, the drag coefficient C_s of a single sphere moving in a thixotropic fluid is determined by three competing factors: shear-induced structure breakdown, the Brownian recovery of the structure, and the convection of the broken fluid microstructure from the sphere front to its wake [11]. The equilibrium of these three competing factors is well-characterized by the normalized velocity $U^*=k_dU/k_a a$. As U^* increases, C_s of a single sphere begins to decrease from one and converges to another value owing to the balance of the convection and shear-induced breakdown effect.

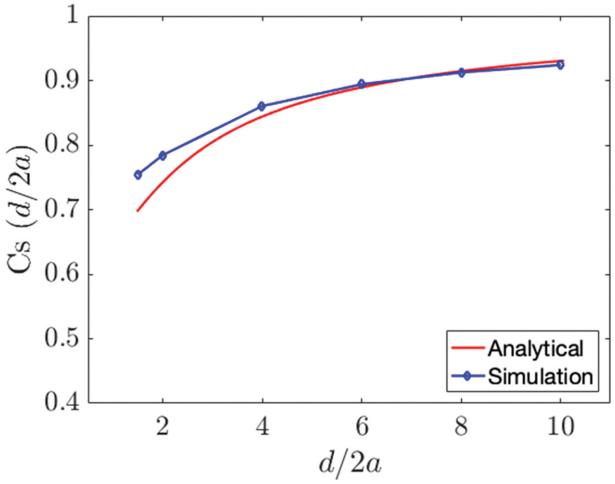

Fig. 3. Drag coefficient as a function of the distance parameter d/2a in a Newtonian fluid at infinite domain. In Newtonian fluids, the drag coefficients of the front and back sphere are exactly same. The case d/2a→∞ equals to a single sphere case. The slight mismatch between analytical and simulated values at d/2a<4 is attributed to the finite computational domain L_0=H_0=160a.

In our two-sphere system in the thixotropy medium, the C_s of each sphere depends both on the geometrical relation between the particles and fluid thixotropy. Therefore, we will investigate the trends of C_s in terms of two dimensionless parameters: the distance parameter d/2a and the Peclet number, which we define as

$$\mathrm{Pe}=\frac{U}{k_a d}. \quad (15)$$

Note that the Pe compares the time scales of convection U/d between the two spheres and Brownian recovery k_a. Here, the definition of the Pe in Eq. (3) is distinguished from that of colloidal suspension ($\mathrm{Pe}_{suspension}=\frac{\dot{\gamma}a^2}{D}$) in that the diffusive momentum transport rate is implicitly represented in the form of k_a rather than diffusion coefficient *D*. For a non-small Pe value, material thixotropy additionally influences C_s of each sphere, because it induces a front-back asymmetric flow solution. We interpret this behavior as thixotropic-hydrodynamic interaction between the two spheres.

4. Finite-element Analysis

We summarize next the numerical method used in our parametric study. Each sphere had radius a=0.025 m and was separated by a distance d that varied from 0.2 to 0.5 m depending on the case. Although we assumed an infinitely large space filled with thixotropic fluid, it was impractical to extend the exterior dimensions L and H to infinity in the simulation. Hence, the computational domain was cut off by a finite but large length L_0=H_0=160a=40d. It is generally known that the perturbation of Newtonian Stokes uniform flow, i.e., **u**=(U, 0), by a single sphere decreases by a factor of 1/*l*, where *l* is the distance from the sphere center to a point **x** normalized by the sphere radius a [23]. Assuming the same decaying scale, the perturbed velocity $\delta\mathbf{u}$ induced from artificially forcing the finite space was negligibly small, with an order of O(1.0%). In the case of a single sphere in a Newtonian fluid, this artificial side wall resulted in the correction factor K(2a/H_0)=1.027 in Eq. (12). We also confirmed that the simulation results did not change with the further increase in the exterior dimensions L_0 and H_0.

The governing equations shown in Eqs. (5), (6), and (7) were numerically solved via quadrilateral finite-element discretization built in the deal.II simulation toolkit [25]. Second-order Taylor-Hood elements were used to discretize the flow variables: two velocity components (u_x, u_r) and pressure p [26]. Additionally, second-order Lagrange polynomial elements were used to discretize the structure parameter λ.

To linearize the system for an iterative solution, the structure-kinetics equation was decoupled from other equations. Picard iterations were implemented in the typical manner: for each k step, the incompressible flow ($\mathbf{u}^{k+1}$, p^{k+1}) was solved with λ^k from the previous iterations, as follows:

$$\nabla\cdot([\eta_\infty+\eta_{str}\lambda^k]\dot{\gamma}^{k+1})-\nabla p^{k+1}=0, \quad (16)$$

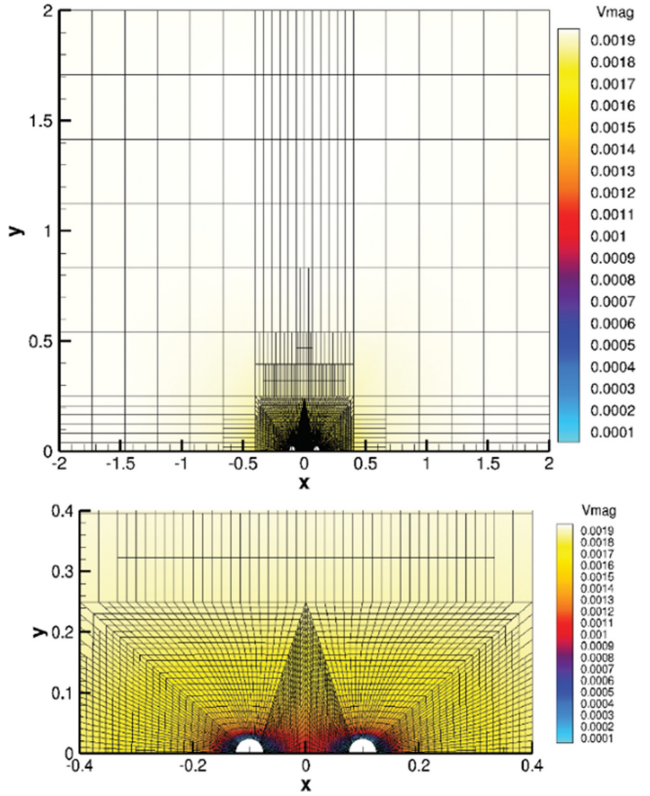

Fig. 4. Computational mesh created by GMSH [28]. Region around the two spheres was adaptively refined for more accurate and efficient simulation. The color represents the magnitude of velocity $|\mathbf{u}|=\sqrt{(\mathbf{u}_x)^2+(\mathbf{u}_r)^2}$.

$$\nabla\cdot\mathbf{u}^{k+1}=0. \tag{17}$$

Subsequently, the structure parameter λ^{k+1} was updated according to

$$\mathbf{u}^{k+1}\cdot\nabla\lambda^{k+1}+k_d\dot{\gamma}_s\lambda^{k+1}-k_a(1-\lambda^{k+1})=0. \tag{18}$$

Solving the advection Eq. (18) using the standard finite element method resulted in insufficient regularity perpendicular to the advection direction **u**. To address this difficulty, we employed the streamline-diffusion stabilization [27].

To guarantee the convergence of the iterative method, an adaptive mesh refinement algorithm in deal.II was used. An initial mesh with 432 elements was created using GMSH [28] and adaptively refined using the criterion $\dot{\gamma}_s$ averaged for each element. After the top 50% mesh was refined in the first refinement step, the top 10% mesh was isotropically refined in the next four steps. The resulting mesh (shown in Fig. 4) contained a total of 3,957 elements, yielding a total of 40,014 degrees of freedom for each second-order element u_x, u_r, and λ, and 18,473 degrees of freedom for p. Solution transfers from coarse to refined mesh facilitated the convergence of the standard GMRES solver [29]. Typically, only k≤10 iterations yielded 10^{-6} relative convergence for the L_2-norm of the solution.

RESULTS AND DISCUSSION

We now discuss the parametric analysis of the simulation results

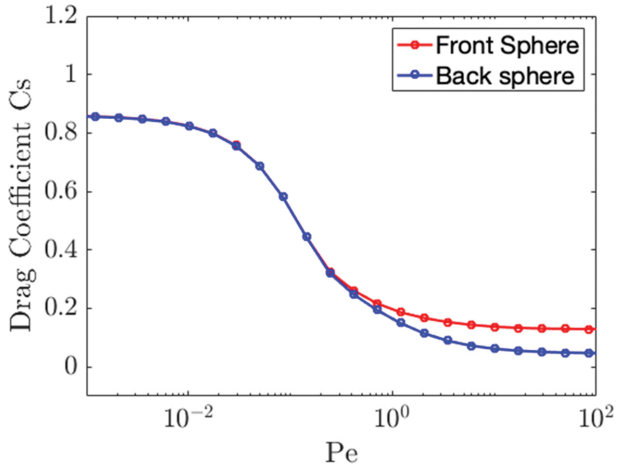

Fig. 5. Drag Coefficient of the front and back sphere as a function of Pe.

in terms of the three dimensionless numbers: the Peclet number (Pe), distance parameter (d/2a), and drag coefficients (C_s). In the simulation, Pe was controlled by changing U in the boundary condition (Eq. (9)). Multiple finite-element meshes were employed to control the distance parameter. All meshes had different values of d, whereas the size of the computational domain Ω remained the same: $L_0=H_0=160a$.

1. Drag Coefficient of Each Sphere at Fixed Distance

We first discuss the trends in the drag coefficient C_s of two spheres separated at a fixed distance d/2a=4. The C_s values of the front and back spheres were plotted as a function of the Peclet number in Fig. 5. Both of the two curves exhibit a sigmoid shape with two asymptotic values at Pe→0 and Pe→∞. Whereas the C_s of the two spheres were the same for low Pe values, the front sphere experiencing larger resistance than the back sphere as Pe increases. The non-equal C_s values of the two spheres, which do not occur for in a Newtonian fluid, are attributed to the thixotropic interactions between the two spheres.

The trends observed in the C_s-Pe curve can be discussed in detail, based on the structure λ-solution at four different values of Pe (=0.01, 0.1, 1.0 and 10). Fig. 6 shows the structure solutions $\lambda(\mathbf{x})$ and the streamlines changed according to the variation in Pe. At low Pe (=0.01), the structure λ was barely disrupted as the Brownian build-up dominated over the structure breakdown caused by the small shear rate near the sphere. Consequently, the thixotropic fluid showed Newtonian-fluid-like behavior solely affected by geometrical hydrodynamic interactions. The flow solution, which is represented by the streamlines in Fig. 6(a), maintained front-and-back symmetry as in the Newtonian fluid case. Moreover, the drag coefficient value of the two spheres corresponded to that of the Newtonian fluid (=0.8441 calculated from the Eq. (14) with d/2a=4) that did not incorporate thixotropy.

In the case of Pe=0.1, as shown in Fig. 6(b), a disrupted structure was observed in the vicinity of the two spheres. However, the flow and structure solutions around the two spheres were still almost identical. This indicates that whereas the thixotropic effect occurred around the two spheres, it was locally manifested around

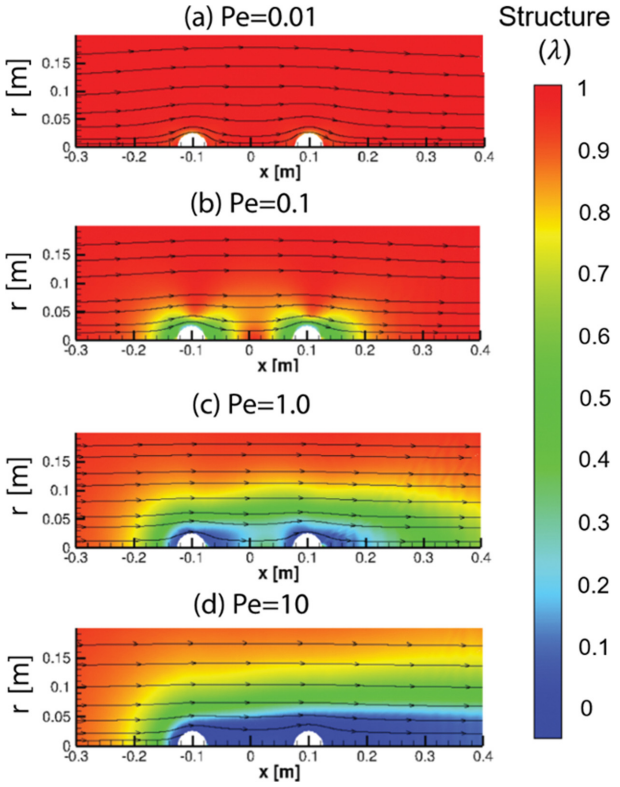

Fig. 6. Structure solution profiles at different Pe numbers Pe=0.01, 0.1, 1.0 and 10.

each sphere without affecting each other. This is because the time scale of convection was sufficiently large for the fluid to recover the internal structures, before reaching the second sphere. Therefore, the C_s values of the two spheres still coincided, although the value itself deviated from that of the Newtonian because of the local thixotropic effect.

When Pe=1.0, the high shear rate around the sphere and the fast convection resulted in front-and-back asymmetry in the structure solution, as demonstrated in Fig. 6(c). As a result of fast convection, the thixotropic fluid disrupted by the front sphere could not recover the initial fully structured state, before it arrived at the second sphere. Hence, the thixotropy affected on a larger length scale, and this global thixotropy effect contributed to the hydrodynamic interaction between the two spheres. Owing to the global thixotropy, the second sphere experienced more broken (or more accumulated shear history) flows, thereby resulting in the lower C_s value of the back sphere at Pe=1 as shown in Fig. 5.

In Fig. 6(d) with Pe=10, we observed that both of the spheres were completely covered by the fully broken structure $\lambda(\mathbf{x})=0$, represented by the region in blue. The C_s values of the two spheres converged to different asymptotical values of 0.129 and 0.046. At a large Pe, the structure rebuilt by thermal motion was insignificant compared to the convection and shear induced breakdown that increased linearly with U. Therefore, the convergence at the large Pe was attributed to the balance between the convection of the microstructure and the shear-induced breakdown. The balance of the back sphere was established at a smaller C_s, as a result of the convection of the more broken thixotropic fluid.

2. Drag Coefficient Change in Two-dimensional Parametric Space of Distance and Pe

We extend our parametric study to incorporate the effect of distance parameter combined with Pe. Additional numerical calculations were conducted using finite-element meshes of different distances, i.e., d/2a=2, 3, 4…10. Herein, the C_s values of front and back spheres are visualized in the form of a contour map, whose ordinate and abscissa are given as Pe and d/2a respectively, as shown in Fig. 7. Overall, the trends of the C_s values were similar for the front and back spheres. The contour variation in the vertical direction (Pe changed while d/2a remained constant) was discussed in the previous part. The C_s transition in the horizontal

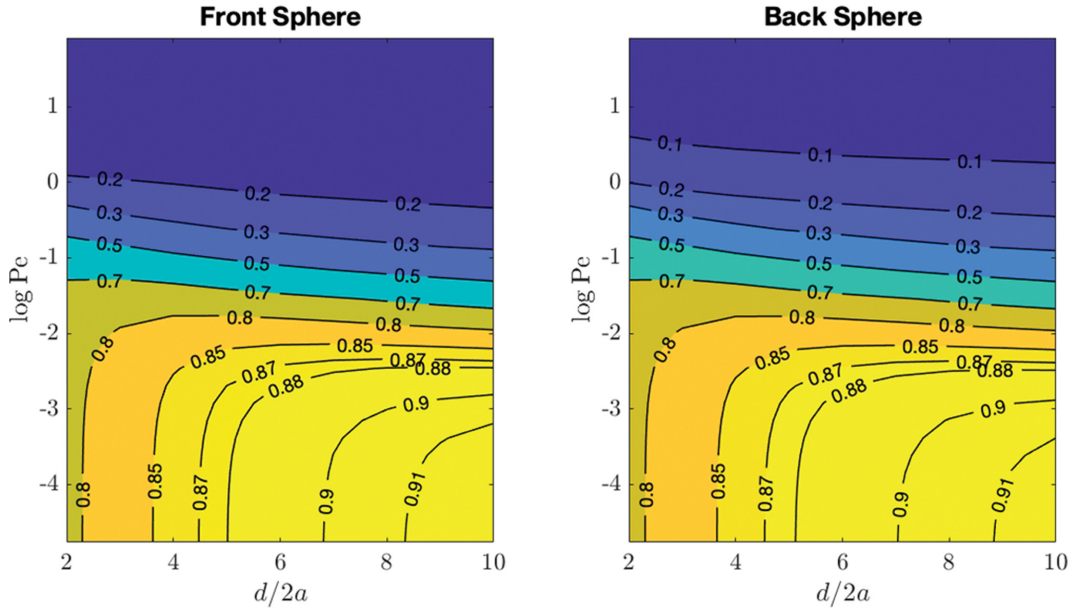

Fig. 7. Drag coefficient of the front and back sphere as a function of the Peclet number and the normalized distance between the two spheres.

direction (d/2a changed while Pe remained constant) varied depending on the Pe number. At low Pe, the C_s of both spheres increased as d/2a increased. As discussed earlier, the geometrical hydrodynamic interaction was a crucial factor at low Pe, where the thixotropic fluid behaved like a Newtonian fluid. The geometrical hydrodynamic interaction, which aids the motion of each other, became insignificant, resulting in the increased C_s of both spheres at a larger distance, as shown in Fig. 3. Therefore, the C_s transition at low Pe can be regarded as the geometrical hydrodynamic interaction change based on the distance change. At high Pe flows, we did not observe any variation in the C_s value with respect to changes in d/2a. This indicates that the thixotropy effect around each sphere dominated over the geometrical hydrodynamic interaction.

As discussed previously, C_s-difference between the two spheres implies an unique thixotropic-hydrodynamic interaction that is distinct from that of a Newtonian fluid. To analyze hydrodynamic interaction change based on the distance and Pe in detail, we investigated the C_s-difference between the two spheres (Cs_{front}–Cs_{back}>0), as shown in Fig. 8. In the previous part, it was shown that the hydrodynamic interaction in the low Pe regime exhibited local thixotropy limited around each sphere. The local thixotropy resulted in the front-back symmetry of the flow that is responsible for the identical C_s values of the front and back spheres. Fig. 8 shows a negligible C_s-difference at low Pe, regardless of the distance d/2a. This implies that the hydrodynamic interaction at low Pe manifests itself in the form of local thixotropy at all distances. It is noteworthy that the identical C_s values at exceedingly small Pe were owing to the Newtonian like behavior rather than the local thixotropy.

When Pe was not too small (>0.3), a distinguishable C_s-difference was observed, as shown in Fig. 8. This is attributable to the global thixotropy effect, which results in relatively small C_s of the trailing second particle. The C_s-difference transition in the vertical direction (increasing Pe with fixed d/2a) can be easily understood in the same manner as the discussion in the previous part. However, the C_s-difference transition in the horizontal direction (increasing d/2a with fixed Pe) is complicated and requires further explanation. In the relatively large Pe regime (1<Pe<10), the C_s-difference remained stationary regardless of d/2a. According to the previous discussion, the structural recovery was insignificant compared with convection and shear-induced breakdown at this large Pe, because a rapid flow shortened the available time for structural recovery. Thus, the constant C_s-difference regardless of d/2a can be regarded as a result of the weakened structure recovery effect at large Pe. However, note that the C_s-difference increased along with the increase in d/2a at larger Pe (>10). This is a counterintuitive result, as it is conjectured that strong convection in a large Pe flow may eliminate the effect of the distance d/2a. Moreover, if the increase in d/2a still influences C_s, a longer recovery time will be enabled; consequently, the drag of the back sphere will increase (C_s-difference will decrease).

To understand the complicated C_s-difference change based on the distance at large Pe value (>10), we investigated the flow field more comprehensively. Fig. 9 shows a contrast of the structure λ and the normalized radial velocity u_r/U (by the strength of the external flow U) at two different distances of d/2a=4 and 10, in the case of Pe=280. The magnitude of the radial velocity around the front sphere, as shown in Fig. 9(b), is noteworthy. The velocity field shows that the thixotropic fluid broken by the front sphere flowed pri-

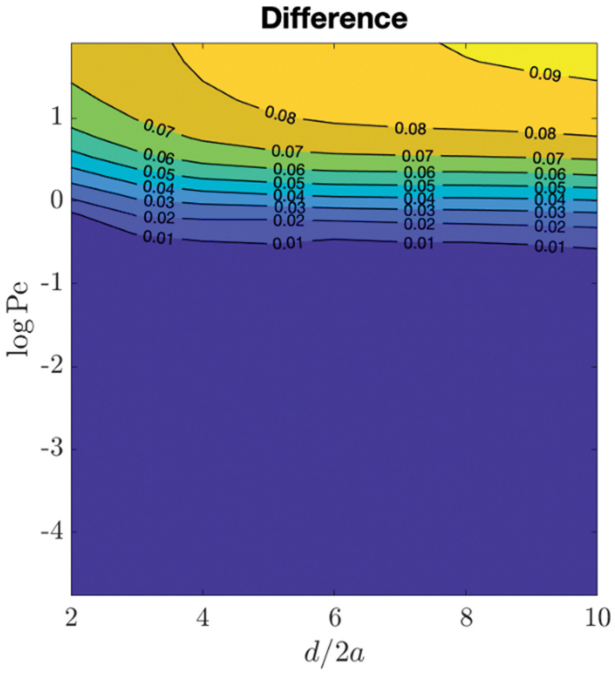

Fig. 8. Drag coefficient difference (Cs_{front}–Cs_{back}) of the front and back spheres as a function of the Peclet number and the normalized distance between the two spheres.

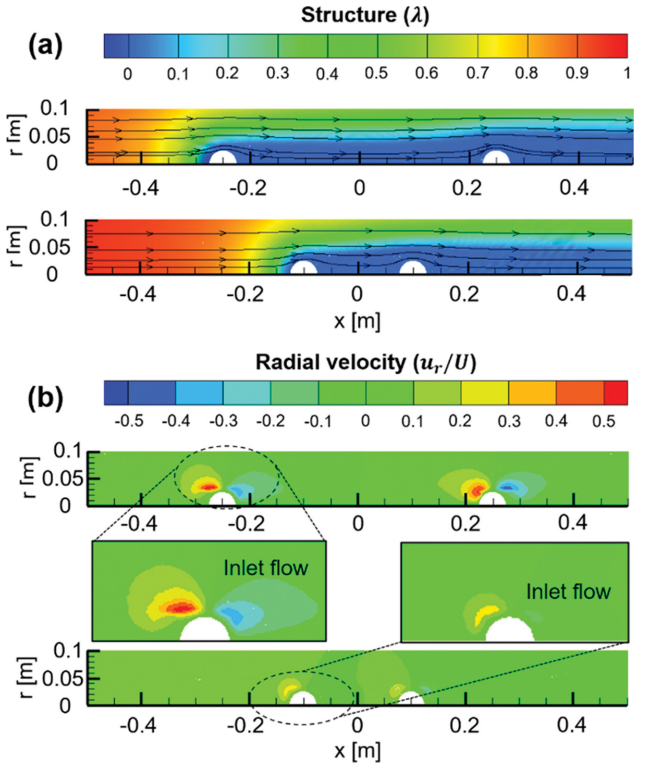

Fig. 9. Structure and radial velocity (u_r/U) solutions of large Pe (=280) thixotropic flow at two different distances (d/2a=4, 10).

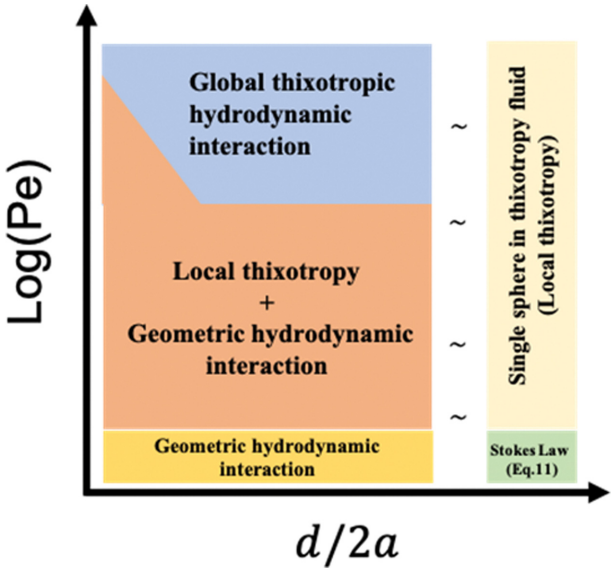

Fig. 10. Conceptual map summarizing different hydrodynamic interaction types in the presence of thixotropy and geometrical factors.

marily into the wake region behind the front sphere, when the distance between the two spheres was larger. As the more broken fluid flowed into the wake region, the second sphere experienced a further reduction in resistance. This result implies that the global thixotropy effect at large Pe can depend significantly on a specific velocity field; this should be investigated in future studies.

To summarize our parametric analysis in this work, we constructed a conceptual map that shows different types of hydrodynamic interactions as a function of Pe and the distance parameter in Fig. 10. At the bottom, where Pe is exceedingly small, the thixotropic property is rarely manifested, and the Newtonian behavior incorporated with geometric hydrodynamic interaction is observed. This will converge to the Stokes law behavior at very large distances ($d/2a \rightarrow \infty$). At a larger Pe, two different types of thixotropic interaction are identified. First, a combination of the thixotropic behavior and geometric hydrodynamic interaction is observed at intermediate Pe. In this regime, where the microstructure of the fluid can be recovered during the convection process, the thixotropic behavior exhibits local thixotropy that is confined to locally to each geometrical element (spheres). In the high Pe regime, the shear history due to the front sphere significantly affects the trailing sphere. This is defined as global thixotropy. It has been shown that the global thixotropy is dependent on a specific flow field. At an infinitely large distance ($d/2a \rightarrow \infty$), all of these thixotropic behaviors can be assumed to exhibit local thixotropy around a single sphere.

CONCLUSION

We performed a parametric study on a purely viscous thixotropic fluid flow around two sequentially aligned spheres. Numerical simulation was conducted using a standard Galerkin finite element method with streamline-diffusion stabilization. Three relevant dimensionless numbers were considered in the parametric analysis: the Peclet number, distance parameter, and drag coefficient. In the first part of the study, the drag coefficient of each sphere was investigated at ranges of Pe values, while the distance parameter was fixed. At small Pe, the thixotropic effect did not manifest as a result of the overwhelming structure recovery effect and Newtonian behavior was observed. As Pe increased, the thixotropic effect first appeared locally around each sphere. A further increase in Pe broke the front-back symmetry flow and resulted in an interesting feature of thixotropic-hydrodynamic interactions between the two spheres, defined as the global thixotropic interaction. In the presence of the global thixotropic interaction, the trailing sphere experiences further reduction in its resistance, owing to microstructures broken by the first sphere. Subsequently, a parametric study was extended to include the distance parameter effect. By investigating drag-difference between the front and back spheres in ranges of Pe and distance conditions, the thixotropic-hydrodynamic interaction between spheres was categorized into three different types: geometric hydrodynamic, combined local thixotropy and geometric hydrodynamic, and global thixotropic-hydrodynamic interactions.

The results of current study are expected to facilitate the understanding of thixotropic fluid flows in complicated flow scenarios, as well as benefit industrial processes involving thixotropic fluids, such as coating and printing. Ultimately, the process or material design and operation condition, which are intricately linked to thixotropy, are expected to be optimized with further elaborated numerical study based on the concept in this paper.

ACKNOWLEDGEMENTS

J.D. Park acknowledges support of the National Research Foundation of Korean (NRF) grant funded by the Korean government (MSIT) (No. NRF-2018R1A5A1024127).

REFERENCES

1. J. Mewis and N. J. Wagner, *Colloidal suspension rheology*, Cambridge University Press, Cambridge (2011).
2. C. F. Goodeve, *Trans. Faraday Soc.*, **35**, 342 (1939).
3. F. Moore, *Trans. J. Br. Ceram. Soc.*, **58**, 470 (1959).
4. J. Stickel, R. J. Phillips and R. L. Powell, *J. Rheol.*, **50**, 379 (2006).
5. J. D. Goddard, *J. Non-Newtonian Fluid Mech.*, **14**, 141 (1984).
6. P. D. Patel and W. B. Russel, *Colloids Surf.*, **31**, 355 (1988).
7. A. A. Potanin, *J. Colloid Interface Sci.*, **145**, 140 (1991).
8. H. A. Barnes, *J. Non-Newtonian Fluid Mech.*, **70**, 1 (1997).
9. J. E. López-Aguilar, M. F Webster, H. R. Tamaddon-Jahoromi and O. Manero, *Rheol. Acta*, **55**, 197 (2016).
10. J. J. Derksen, *Appl. Math. Model*, **35**, 1656 (2011).
11. J. Kim and J. D. Park, *Appl. Math. Model.*, **82**, 848 (2020).
12. J. E. López-Aguilar, M. F Webster, H. R. Tamaddon-Jahoromi and O. Manero, *Rheol. Acta*, **54**, 307 (2014).
13. L. Ouyang, Z. Wu, J. Wang, X. Qi, Q. Li, J. Wang and S. Lu, *RSC Adv.*, **10**, 19360 (2020).
14. K. Shikinaka, N. Taki, K. Kaneda and Y. Tominaga, *Chem. Comm.*, **53**, 613 (2016).
15. M. T. Balhoff and K. E. Thompson, *Chem. Eng. Sci.*, **61**, 698 (2006).
16. M. T. Balhoff and K. E. Thompson, *AIChE J.*, **50**, 3034 (2004).

17. K. H. Kim and H. N. Chang, *Biotechnol. Bioeng.*, **28**, 452 (1986).
18. J. Engmann and A. S. Burbidge, *Food Fucnt.*, **4**, 443 (2013).
19. D. Quemada and R. Droz, *Biorhelogy*, **20**, 635 (1983).
20. R. G. de Krester and D. V. Boger, *Rheol. Acta*, **40**, 582 (2001).
21. N. Zanna and C. Tomasini, *Gels*, **3**, 39 (2017).
22. S. Mortazavi-Manesh and J. M. Shaw, *Energy Fuels*, **28**, 972 (2014).
23. J. Happel and H. Brenner, *Low Reynolds number hydrodynamics*, Prentice-Hall, London (1965).
24. M. Stimson and G. B. Jeffrey. *Proc. R. Soc. Lond. Series A*, **111**, 110 (1926).
25. D. Arndt, W. Bangerth, D. Davydov, T. Heister, L. Heltai, M. Kronbichler, M. Maier, J. P. Pelteret, B. Turcksin and D. Wells, *J. Numer. Math.*, **25**, 137 (2017).
26. C. Taylor and P. Hood, *Comput. Fluids*, **1**, 73 (1973).
27. A. N. Brooks and T. J. R. Hughes, *Comput. Methods in Appl. Mech. Eng.*, **32**, 199 (1982).
28. C. Geuzaine and J. F. Remacle, *Int. J. Numer. Eng.*, **79**, 1309 (2009).
29. Y. Saad and M. H. Schultz, *SIAM J. Sci. and Stat. Comp.*, **7**, 856 (1986).